Numerical simulation of a truncated cladding negative curvature fiber sensor based on the surface plasmon resonance effect

Zhichao Zhang(张志超)[1], Jinhui Yuan(苑金辉)[1,2,†], Shi Qiu(邱石)[1], Guiyao Zhou(周桂耀)[3], Xian Zhou(周娴)[2], Binbin Yan(颜玢玢)[1], Qiang Wu(吴强)[4,5,‡], Kuiru Wang(王葵如)[1], and Xinzhu Sang(桑新柱)[1]

[1] *State Key Laboratory of Information Photonics and Optical Communications, Beijing University of Posts and Telecommunications, Beijing* 100876, *China*
[2] *Research Center for Convergence Networks and Ubiquitous Services, University of Science & Technology Beijing, Beijing* 100083, *China*
[3] *Guangzhou Key Laboratory for Special Fiber Photonic Devices, South China Normal University, Guangzhou* 510006, *China*
[4] *Department of Physics and Electrical Engineering, Northumbria University, Newcastle upon Tyne, NE*1 8*ST, United Kingdom*
[5] *Key Laboratory of Nondestructive Test (Ministry of Education), Nanchang Hong Kong University, Nanchang* 330063, *China*

(Received 23 February 2022; revised manuscript received 15 May 2022; accepted manuscript online 14 June 2022)

A refractive index (RI) sensor based on the surface plasmon resonance effect is proposed using a truncated cladding negative curvature fiber (TC-NCF). The influences of the TC-NCF structure parameters on the sensing performances are investigated and compared with the traditional NCF. The simulation results show that the proposed TC-NCF RI sensor has an ultra-wide detection range from 1.16 to 1.43. The maximum wavelength sensitivity reaches 12400 nm/RIU, and the corresponding R^2 of the polynomial fitting equation is 0.9999. The maximum and minimum resolutions are 2.56×10^{-5} and 8.06×10^{-6}, respectively. In addition, the maximum amplitude sensitivity can reach -379.1 RIU^{-1} when the RI is chosen as 1.43. The proposed TC-NCF RI sensor could be useful in biochemical medicine, environmental monitoring, and food safety.

Keywords: truncated cladding negative curvature fiber, refractive index sensor, surface plasmon resonance

PACS: 42.81.Pa **DOI:** 10.1088/1674-1056/ac785e

1. Introduction

Anti-resonant hollow-core negative curvature fibers (HC-NCFs) have attracted the attention of many researchers. HC-NCFs have simple cladding structures, which usually consist of only one layer of glass tube rings. For the boundary of the hollow-core, the surface of the tube rings is designed with a negative curvature, which can inhibit the coupling between the core modes and cladding modes in the case of wavenumber mismatch.[1,2] HC-NCFs have been demonstrated with low transmission losses due to the inhibited mode coupling.[3–5] Profitably, HC-NCFs can overcome the inevitable attenuation caused by glass scattering. In addition, HC-NCFs have a wide range of applications by taking advantage of their broad transmission windows. Particularly, benefited by their large hollow core, HC-NCFs can be easily filled with liquid and gas, which gives them potential applications in the field of sensing.[6–9]

The surface plasmon resonance (SPR) effect can be used to enhance the sensitivity of optical fiber sensors.[10] The longitudinal oscillation of free electrons on the metal surface generates the surface plasmon wave (SPW). It is highly influenced by the refractive index (RI) of the surrounding environment; therefore, the SPR effect can be applied in RI sensing. The SPR effect will occur when the phase-matching conditions between the incident light wave and SPW are satisfied.[11] As a result, the energy of the core mode will couple with the SPW, and the confinement loss of the core mode will increase dramatically at the resonant wavelength. In 2006, Hassani *et al.* proposed an SPR-based microstructured fiber RI sensor and investigated the coupling mechanism between the core mode and surface plasmon polariton (SPP) mode.[12] In 2017, Ding *et al.* reported an SPR RI sensor based on a tapered coreless fiber, where the wavelength sensitivity of the proposed sensor was 2278.4 nm/RIU in the RI range of 1.33–1.39.[13] In 2020, Yu *et al.* proposed a D-shaped silicon core fiber sensor based on the SPR effect, and the sensor achieved an average sensitivity of 2650 nm/RIU in the RI range of 1.25–1.6.[14] In 2020, Qiu *et al.* proposed a HC-NCF with high birefringence for low RI sensing in the RI range of 1.20–1.34, and the obtained maximum sensitivity was -5700 nm/RIU.[15] At present, the reported RI sensors have low sensitivity and a narrow RI detection range, which greatly limit their practical applications. To our knowledge, HC-NCF sensors with high sensitivity and wide RI detection ranges have not been reported yet.

With the traditional SPR-based microstructured fiber, the cladding structure is generally more complex. In contrast, the cladding structure of the HC-NCFs includes only one layer of tubes, and a high intensity evanescent field on the interface between the fiber core and tubes can be generated. The evanescent field provides possible conditions for stimulating the SPR effect. RI sensors based on HC-NCFs can detect the RI of

[†]Corresponding author. E-mail: yuanjinhui81@bupt.edu.cn
[‡]Corresponding author. E-mail: qiang.wu@northumbria.ac.uk

© 2023 Chinese Physical Society and IOP Publishing Ltd

the analyte through the interaction between the core mode and analyte. Therefore, an effective method to improve the sensing sensitivity is to expand the area of interaction between the core mode and analyte by reasonable design of the core and cladding structures and sizes of the HC-NCFs. In this paper, we propose a truncated cladding negative curvature fiber (TC-NCF) for RI sensing based on the SPR effect. Unlike traditional HC-NCFs, the cladding region of the proposed TC-NCF has six silica tubes covering a portion of the entire circle. Gold wires fill the two opposite tubes along the y-axis. The remaining four tubes and hollow-core are filled with the gaseous or liquid analytes. Such a truncated design can further reduce the leakage loss.[16] Moreover, by keeping the ratio of the tube diameter to the core diameter constant, a larger proportion of the fiber core can be provided to increase the interaction area between the analyte and core mode compared with the un-truncated HC-NCFs, thus improving the wavelength sensitivity of the sensor. The proposed TC-NCF RI sensor has an RI detection range of 1.16 to 1.43 together with maximum sensitivity of 12400 nm/RIU.

2. Design of the TC-NCF and theory

The cross-sectional structure of the proposed TC-NCF is shown in Fig. 1(a), where the yellow, green, and gray regions represent the gold, gaseous or liquid analyte, and silica, respectively. The black dashed lines represent the circle, where the centers of the six tubes are located. The cladding structure of the TC-NCF consists of six truncated silica tubes that are two-thirds the size of the entire circle. The gold fills the two opposite tubes along the y-axis. The analyte is poured into the remaining areas (four tubes and the hollow core). The six silica tubes are the same size, the cladding circle's radius is set to $r = 13.5$ μm, and the tubes' thickness is set to $t = 0.8$ μm. The core region's radius is set to $R = 15$ μm. The structure parameters used here are the optimal values. As shown in Figs. 1(b) and 1(c), the fundamental modes are well confined to the core region of the TC-NCF due to the anti-resonance effect and inhibitory coupling.

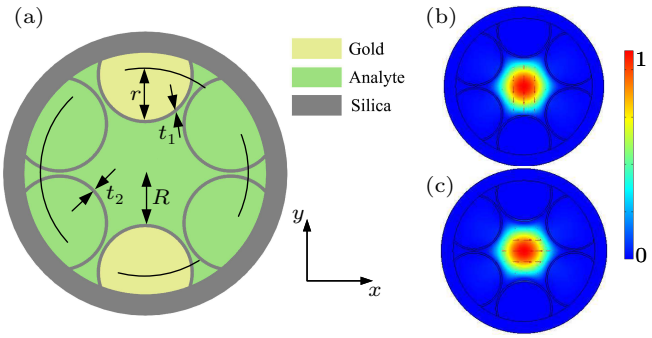


Fig. 1. (a) The cross-sectional structure of the proposed TC-NCF. (b) and (c) The mode field distributions of y-pol core mode and x-pol core mode of the TC-NCF calculated at a wavelength of 1.3 μm, respectively. The RI of the analyte is 1.35.

The SPP mode is the transversally magnetic (TM) mode. For the SPP mode, the magnetic field is distributed at the metal–dielectric interface, and the wave vector of the magnetic field is perpendicular to the direction of propagation. The propagation constant of an SPW at a metal–dielectric interface can be described as

$$\beta_{\mathrm{SPW}} = \frac{\omega}{c}\sqrt{\frac{\varepsilon_{\mathrm{d}}\varepsilon_{\mathrm{m}}}{\varepsilon_{\mathrm{d}}+\varepsilon_{\mathrm{m}}}} = \frac{2\pi}{\lambda}\sqrt{\frac{\varepsilon_{\mathrm{d}}\varepsilon_{\mathrm{m}}}{\varepsilon_{\mathrm{d}}+\varepsilon_{\mathrm{m}}}}, \tag{1}$$

where ω is the angular frequency, c is the light speed in the vacuum, λ is the wavelength in the vacuum, and ε_{d} and ε_{m} are the permittivities of the metal and dielectric, respectively.[17] The permittivity of the dielectric is usually positive, and the real part of metallic permittivity (gold, silver, aluminum, etc.) is negative in the visible and near-infrared spectral regions. Thus, $|\varepsilon_{\mathrm{m}}|$ should be less than $|\varepsilon_{\mathrm{d}}|$ according to Eq. (1).

The permittivity of the gold is expressed as

$$\varepsilon_{\mathrm{m}} = \varepsilon_{\infty} - \frac{\omega_{\mathrm{D}}^2}{\omega(\omega + \mathrm{j}\gamma_{\mathrm{D}})} - \frac{\Delta\varepsilon\cdot\Omega_{\mathrm{L}}^2}{(\omega^2-\Omega_{\mathrm{L}}^2)+\mathrm{j}\Gamma_{\mathrm{L}}\omega}, \tag{2}$$

$$\begin{cases} \varepsilon_{\infty} = 5.9673, \\ \gamma_{\mathrm{D}} = 2\pi\cdot 15.92\ \mathrm{THz}, \\ \omega_{\mathrm{D}} = 2\pi\cdot 2113.6\ \mathrm{THz}, \\ \Delta\varepsilon = 1.09, \\ \Gamma_{\mathrm{L}} = 2\pi\cdot 104.86\ \mathrm{THz}, \\ \Omega_{\mathrm{L}} = 2\pi\cdot 650.07\ \mathrm{THz}, \end{cases} \tag{3}$$

where ε_{∞} is the dielectric constant of high frequency, γ_{D} is the damped frequency, ω_{D} is the frequency of plasma, $\Delta\varepsilon$ is a weighting factor, and Ω_{L} and Γ_{L} are the frequency and spectral width of the Lorentz oscillator, respectively.[11]

According to the Sellmeier equation, the RI of silica can be expressed as[18]

$$n_{\mathrm{silica}}(\lambda) = \sqrt{1 + \frac{A\cdot\lambda^2}{\lambda^2-B^2} + \frac{C\cdot\lambda^2}{\lambda^2-D^2} + \frac{E\cdot\lambda^2}{\lambda^2-F^2}}, \tag{4}$$

$$\begin{cases} A = 0.6961663, \\ B = 0.0684043\ \mu\mathrm{m}, \\ C = 0.4079426, \\ D = 0.1162414\ \mu\mathrm{m}, \\ E = 0.8974794, \\ F = 9.896161\ \mu\mathrm{m}. \end{cases} \tag{5}$$

For the proposed TC-NCF sensor, the evanescent wave of the fundamental mode excites the SPW on the gold surface. The coupling conditions for the fundamental mode and SPP mode are that the propagation constants of the two waves are equal. Because of the strong coupling between the fundamental mode and the SPP mode, the confinement loss will get a sharp peak. The propagation constant of the SPW will change as the RI of the filled analyte changes. The fundamental mode's and SPP mode's resonant wavelengths will change at this time. As

a result, detection of the resonant wavelength yields the analyte's RI. In addition, the coupling strength of the core mode and SPP mode will undergo a change as the RI of the analyte changes, resulting in different confinement losses of the core mode under different analyte RIs.

There are two main methods used to detect the RI of an analyte. The first detects the resonant wavelength. The wavelength sensitivity is defined as[19,20]

$$S_\lambda\ (\mathrm{nm/RIU}) = \frac{\Delta\lambda_{\mathrm{peak}}}{\Delta n_{\mathrm{a}}}, \tag{6}$$

where Δn_{a} is the variation of the RI of the analyte, and $\Delta\lambda_{\mathrm{peak}}$ is the shift of the resonant wavelength due to Δn_{a}.

The corresponding resolution is defined as[21]

$$R\ (\mathrm{RIU}) = \frac{\Delta n_{\mathrm{a}} \cdot \Delta\lambda_{\mathrm{min}}}{\Delta\lambda_{\mathrm{peak}}}, \tag{7}$$

where $\Delta\lambda_{\mathrm{min}} = 0.1$ nm is the wavelength resolution.

The confinement loss of the core mode is expressed as[22]

$$CL\ (\mathrm{dB/cm}) = 8.686 \cdot \frac{2\pi}{\lambda} \cdot \mathrm{Im}(n_{\mathrm{eff}}) \cdot 10^4, \tag{8}$$

where $\mathrm{Im}(n_{\mathrm{eff}})$ is the imaginary of the effective RI.

The second method is based on the detection of the amplitude at a single wavelength. The RI of the analyte is obtained by monitoring the change in transmitted light energy. We define the transmission loss as $\alpha(\lambda, n_{\mathrm{a}})$ and the incident light power as P_0. The light energy P after the propagation becomes[23]

$$P(L,\lambda,n) = P_0\, \mathrm{e}^{-\partial(\lambda,n_{\mathrm{a}})L}. \tag{9}$$

The amplitude sensitivity is defined as

$$S_{\mathrm{A}}(\lambda)\ (\mathrm{RIU}^{-1}) = \frac{(P(L,\lambda,n_{\mathrm{a}}+\Delta n_{\mathrm{a}}) - P(L,\lambda,n_{\mathrm{a}}))/P(L,\lambda,n_{\mathrm{a}})}{\Delta n_{\mathrm{a}}}, \tag{10}$$

where Δn_{a} is the change in n_{a}. The length of the RI sensor is selected as $L = 1/\partial(\lambda, n_{\mathrm{a}})$. Then, the amplitude sensitivity can be simplified as

$$S_{\mathrm{A}}(\lambda)\ (\mathrm{RIU}^{-1}) = \frac{-(\partial\alpha(\lambda,n_{\mathrm{a}})/\partial n_{\mathrm{a}})}{\alpha(\lambda,n_{\mathrm{a}})}. \tag{11}$$

3. The effects of the TC-NCF structure parameters on the propagation characteristics

The propagation characteristics of the proposed TC-NCF are investigated using the finite element method. In the simulation, the boundary conditions are chosen as the perfect matching layer (PML), whose thickness is set as 6 μm, and the mesh size is $\lambda/5$. Because the effective RI difference between the *x*-pol core mode and the SPP mode is so great, the *x*-pol core mode and the SPP mode have no resonance. As a result, we will solely analyze the coupling characteristics between the *y*-pol core mode and the SPP mode in this work.

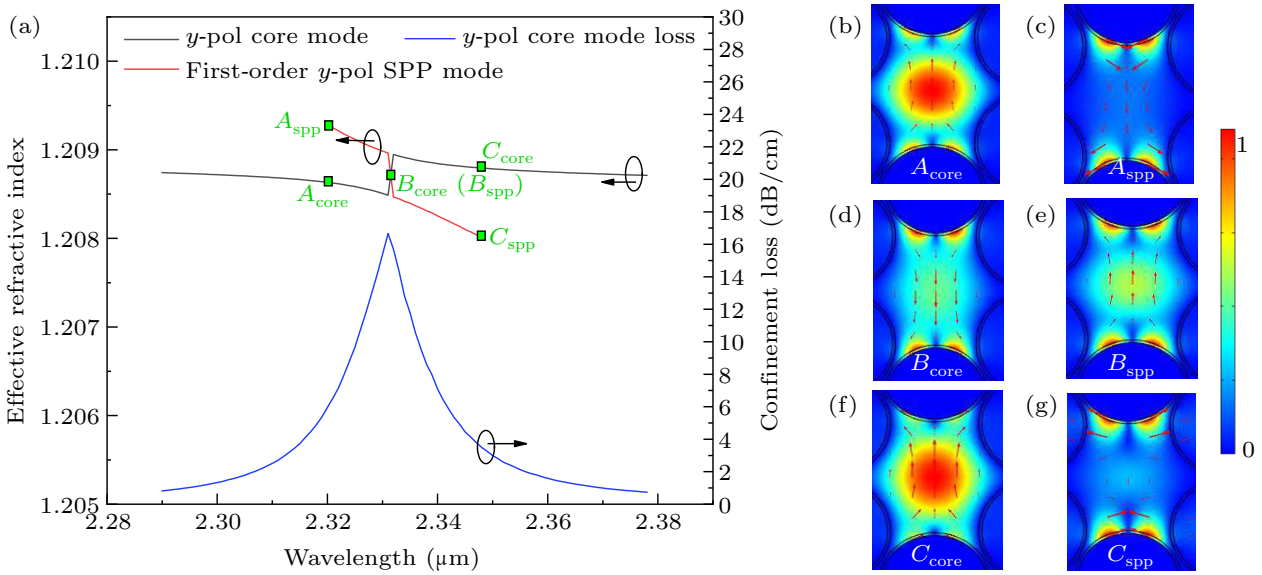


Fig. 2. (a) When the RI of the analyte is set to 1.21, the effective RIs of the *y*-pol core mode (black line) and first-order *y*-pol SPP mode (red line), as well as the confinement loss spectrum of the *y*-pol core mode (blue line) are shown. Here, (b)–(g) correspond to the calculated mode field distributions of A_{core}, A_{spp} at the wavelength 2.320 μm, B_{core}, B_{spp} at the wavelength 2.331 μm, and C_{core}, C_{spp} at the wavelength 2.348 μm, respectively.

When the RI of the analyte is 1.21, the effective RI curves of the *y*-pol core mode and first-order SPP mode, as well as the confinement loss spectrum of the *y*-pol core mode, are shown in Fig. 2(a). The effective RI of the *y*-pol core mode is smaller than that of the first-order *y*-pol SPP mode when the wavelength is shorter than the resonant wavelength. The effective RI of the *y*-pol core mode increases as the wavelength approaches the resonant wavelength, while the effective RI of

the first-order SPP mode decreases significantly, intersecting at the resonant wavelength 2.331 μm. It denotes that the *y*-pol core mode will be coupled to the first-order SPP mode at 2.331 μm wavelength. The effective RI of the *y*-pol core mode is greater than that of the SPP mode at wavelengths longer than the resonant wavelength. Moreover, there is a sharp confinement loss peak at the resonant wavelength 2.331 μm due to the coupling between the *y*-pol core mode and first-order SPP mode. Figures 2(b)–2(g) correspond to the calculated mode field distributions of A_{core}, A_{spp} at the wavelength 2.320 μm, B_{core}, B_{spp} at the wavelength 2.331 μm, and C_{core}, C_{spp} at the wavelength 2.348 μm, respectively. At the position deviating from the resonant wavelength, the energy of the *y*-pol core mode is much greater than that of the SPP mode, and the confinement loss is very small. The closer to the resonant wavelength, the more the energy of the *y*-pol core mode is converted to the SPP mode. When energy is transferred from the *y*-pol core mode to the SPP mode, the sharp confinement loss peak at the resonant wavelength appears, corresponding to the mode field distributions of the two modes shown in Figs. 2(d) and 2(e). Figure 3(a) depicts the confinement loss of the TC-NCF under a 0.01 change in analyte RI when $t_1 = t_2 = 0.8$ μm, $r = 0.9R$, and $R = 13.5$ μm, 15 μm, 16.5 μm, and 18 μm, respectively. When the analyte RI changes from 1.21 to 1.22, the wavelength shift is 44 nm at different R. The change in R has a great influence on the confinement loss. When R is larger, the confinement loss is smaller. This is mainly because a large core is more likely to constrain the light field. In addition, the higher the RI of the analyte, the smaller the confinement loss. To obtain a wider detection range, the confinement loss should not be very small, otherwise the amplitude change of the spectral signal will not be obvious when the analyte RI is high. Figure 3(b) shows the influence of R on the confinement loss with $r = 13.5$ μm. Similarly, the confinement loss decreases with the increase in R. In Fig. 3(c), the resonant wavelengths experience a shift of 44 nm when r is equal to 0.8, 0.85, and 0.9 times R, respectively. Such a relationship has a slight effect on the confinement loss. In Figs. 3(a)–3(c), R has a greater effect on the confinement loss of the *y*-pol core mode compared to r, but they have no effect on the sensitivity of the proposed TC-NCF sensor.

Figure 4(a) shows the effects of the thickness t_1 and t_2 of the silica tubes filled with gold on the confinement loss of the TC-NCF. As t_1 increases from 0.6 μm to 0.8 μm, and to 1 μm, the shift of the resonant wavelength $\Delta\lambda_{\text{peak}}$ increases 9 nm each time. The confinement loss is slightly reduced when t_1 is increased from 0.6 μm to 0.8 μm, but it is greatly reduced when t_1 is 1 μm. This is mainly because the thickness of the silica tubes prevents the coupling between the core mode and SPP mode. Here, t_2 without the gold-filled tubes has no effect on the sensitivity, as shown in Fig. 4(b). The reason for this phenomenon is considered to be due to the fact that t_1 is related to the size of the gold rod, and thus affects the fluctuation of the SPW. However, the size of t_2 has nothing to do with the rod and cannot affect the SPR effect.

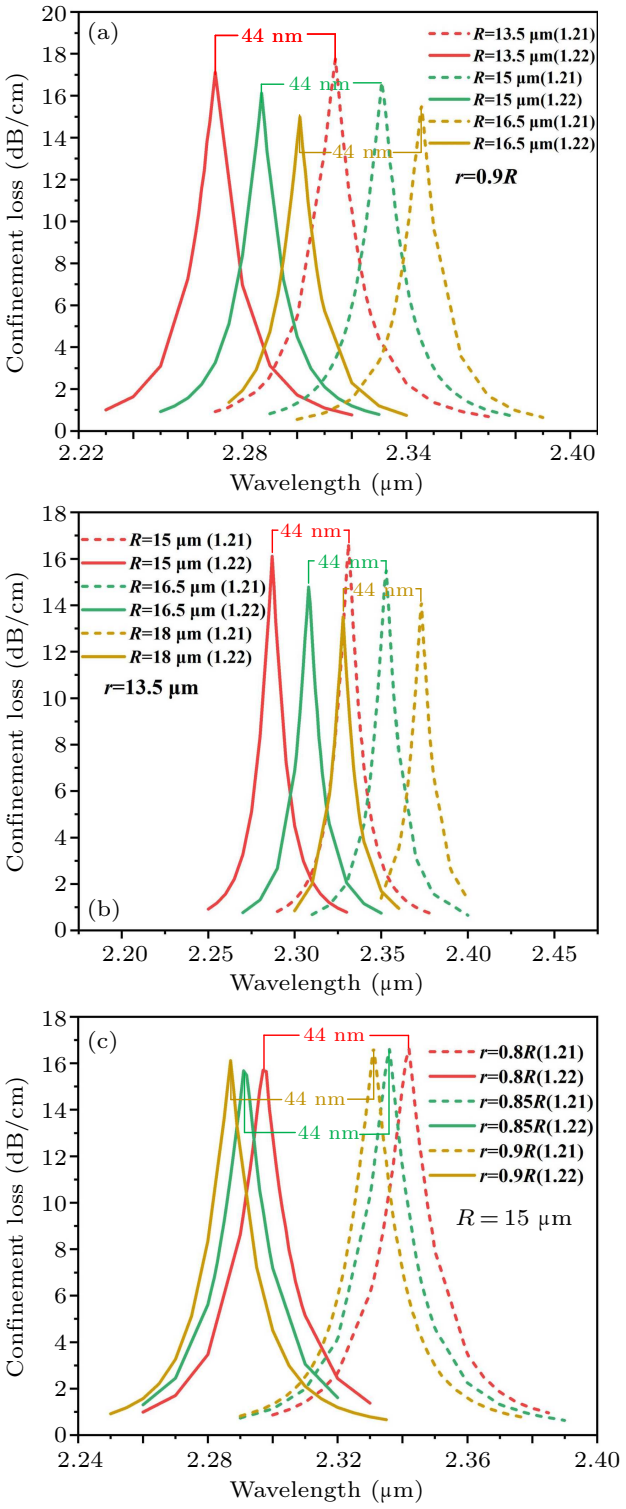


Fig. 3. The confinement loss of the *y*-pol core mode of the TC-NCF as a function of the wavelength. The solid and dashed lines correspond to the analyte RIs of 1.22 and 1.21, respectively. (a) R is chosen as 13.5 μm, 15 μm, and 16.5 μm, respectively, when $r = 0.9R$ and $t = 0.8$ μm; (b) R is chosen as 15 μm, 16.5 μm, and 18 μm, respectively, when $r = 13.5$ μm and $t = 0.8$ μm; (c) r is chosen as $0.8R$, $0.85R$, and $0.9R$, respectively, when $R = 15$ μm and $t = 0.8$ μm.

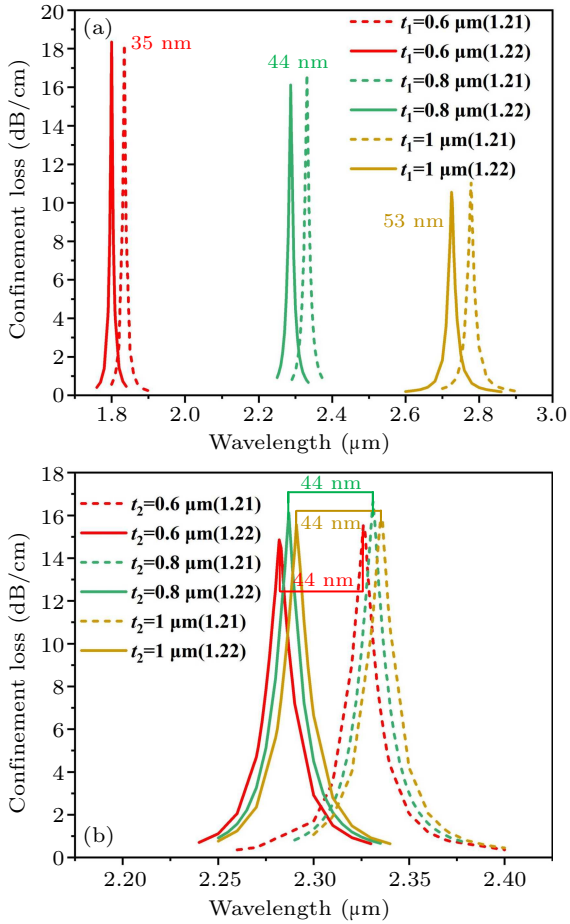


Fig. 4. The confinement loss of the *y*-pol core mode as a function of the wavelength. The solid and dashed lines correspond to the analyte RIs of 1.22 and 1.21, respectively: (a) t_1 is chosen as 0.6 μm, 0.8 μm, and 1 μm, respectively, when R =15 μm, r =13.5 μm, and t_2 =0.8 μm; (b) t_2 is chosen as 0.6 μm, 0.8 μm, and 1 μm, respectively, when R = 15 μm, r =13.5 μm, and t_1 =0.8 μm.

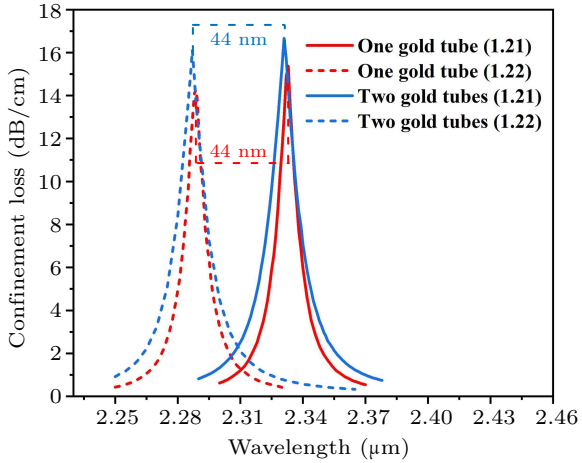


Fig. 5. The confinement loss of the *y*-pol core mode as a function of the wavelength. The solid and dashed lines correspond to the analyte RIs of 1.22 and 1.21, respectively, and the red and blue lines correspond to one and two gold tubes, respectively.

Figure 5 shows the effect of the number of the gold tubes on the confinement loss of the TC-NCF. In Fig. 5, the wavelength shifts of one and two gold tubes are the same, but the confinement loss of the core mode is larger for the two gold tubes, and the resonant wavelengths are slightly blue-shifted. The SPP mode formed by the two metal structures is the supermode, and the coupling between the supermode and core mode is stronger, which is beneficial to obtain a larger signal-to-noise ratio (SNR).

In summary, only t_1 has an effect on the sensitivity of the proposed TC-NCF sensor. To reduce the structure complexity, the six silica tubes in the cladding region are designed with the same thickness of 0.8 μm. The sensitivity of the proposed TC-NCF sensor will be reduced if the thickness is smaller than 0.8 μm, and a large thickness will be limited to a low RI detection range. R also affects the confinement loss of the TC-NCF; therefore, it is designed as 15 μm after considering the RI detection range. The radius r of the cladding tubes and the number of gold tubes have negligible effects on the sensing performance.

4. The effect of the truncation on the sensing performance

We will also analyze the sensing performance of the NCF without the truncation. The cross-sectional structure of the NCF without the truncation is shown in Fig. 6(a). To ensure the same cross-sectional area as that shown in Fig. 1(a), the core diameter (D) and thickness of the cladding tubes (t) are chosen as 26.8 μm and 0.8 μm, respectively, the diameter of the cladding tubes is set as d = 21 μm, and the core diameter is smaller than that of the TC-NCF. Similar to the TC-NCF, the *y*-pol core mode is coupled with the first-order SPP mode when phase matching conditions are satisfied, as shown in Figs. 6(b) and 6(c). Figure 6(d) shows the confinement loss of the TC-NCF and NCF as a function of the wavelength. In Fig. 6(d), the confinement loss of the NCF without truncation is greater than that of the TC-NCF. This is mainly because the TC-NCF has lower loss. Moreover, the $\Delta\lambda_{peak}$ of the TC-NCF is 1 nm larger than that of the NCF without truncation when the analyte RI changes from 1.23 to 1.24. Figure 6(e) shows the confinement loss of the NCF as a function of the wavelength in the RI range from 1.23 to 1.31. Similar to the TC-NCF, the confinement loss of the core mode decreases gradually as the RI of the analyte increases.

The sensitivities of two kinds of fibers in the considered RI range of 1.23–1.31 are shown in Figs. 7(a) and 7(b). The average sensitivities of the TC-NCF and NCF are 5251.67 nm/RIU and 5233.33 nm/RIU, respectively. The average sensitivity of the TC-NCF is 18.34 higher than that of the NCF. Moreover, the Pearson correlation coefficient and R^2 of the proposed TC-NCF are larger than those of the NCF. This phenomenon is consistent with the previous analyses. Compared with the NCF, the TC-NCF has a larger mode field, which leads to a larger overlap space with the analyte and higher sensitivity with the change in the analyte RI.

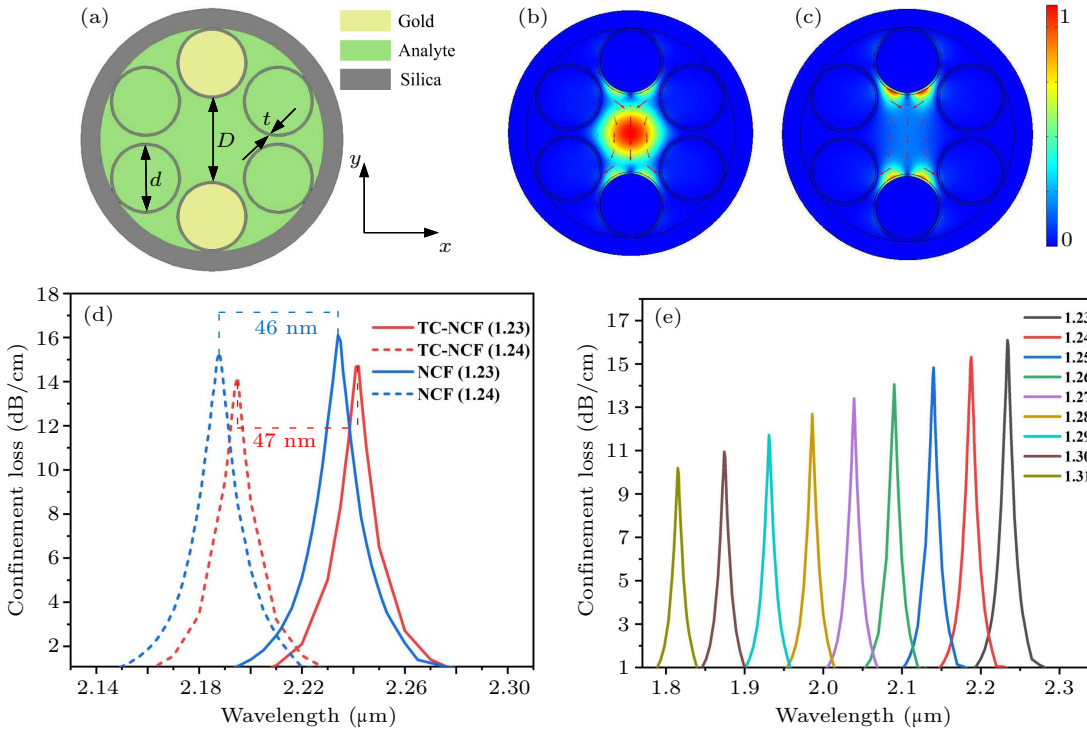


Fig. 6. (a) The cross-sectional structure of the NCF without truncation. (b) and (c) The mode field distributions of the *y*-pol core mode and first-order SPP mode calculated at the wavelength 1.803 μm. (d) The confinement loss of the TC-NCF (red lines) and NCF (blue lines) as functions of the wavelength. The solid and dashed lines correspond to the analyte RIs of 1.23 and 1.24, respectively. (e) The confinement loss of the NCF as a function of the wavelength when the RI changes from 1.23 to 1.31.

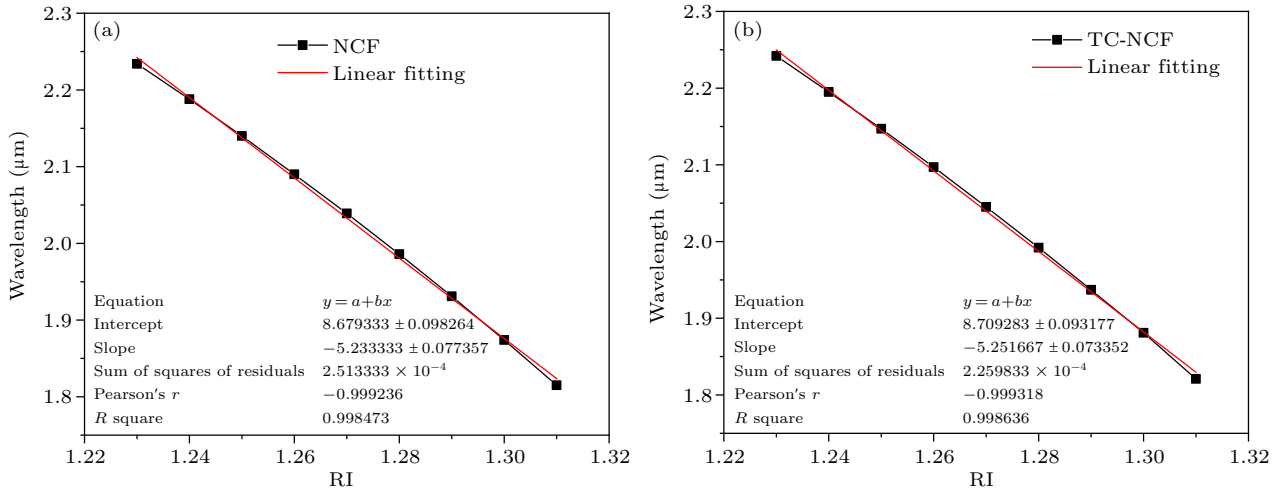


Fig. 7. The resonant wavelengths as a function of the analyte RI (black lines) and linear fitting results (red lines) in (a) the NCF without truncation, and (b) the proposed TC-NCF.

5. Sensing performances of the proposed TC-NCF

Figure 8(a) shows the relationship between the confinement loss of the TC-NCF and the wavelength in the RI range of 1.16–1.43. As the RI increases, the resonant wavelength shifts to the shorter wavelength side and the confinement loss gradually decreases. The effective RI difference between the core mode and the SPP mode is relatively small in the relatively high RI environment, and the phase matching conditions tend to be satisfied at a short wavelength. Also, the energy conversion efficiency between the core mode and the SPP mode is relatively low. Figure 7(b) shows the polynomial relationship between the resonant wavelength and the RI of the analyte based on the results in Fig. 8(a). In Fig. 8(b), the polynomial fitting equation used is $y = 81.35 - 189.72x + 155.27x^2 - 43.35x^3$, and R^2 is 0.9999. The polynomial fitting results show that the maximum RI sensitivity can reach 12400 nm/RIU when the analyte RI changes from 1.42 to 1.43. Figure 8(c) shows the resolution of the TC-NCF sensor in the RI range of 1.16–1.43. With the increase in the RI, the resolution of the TC-NCF sensor gradually decreases. This is mainly because the shift of the resonant wavelengths becomes

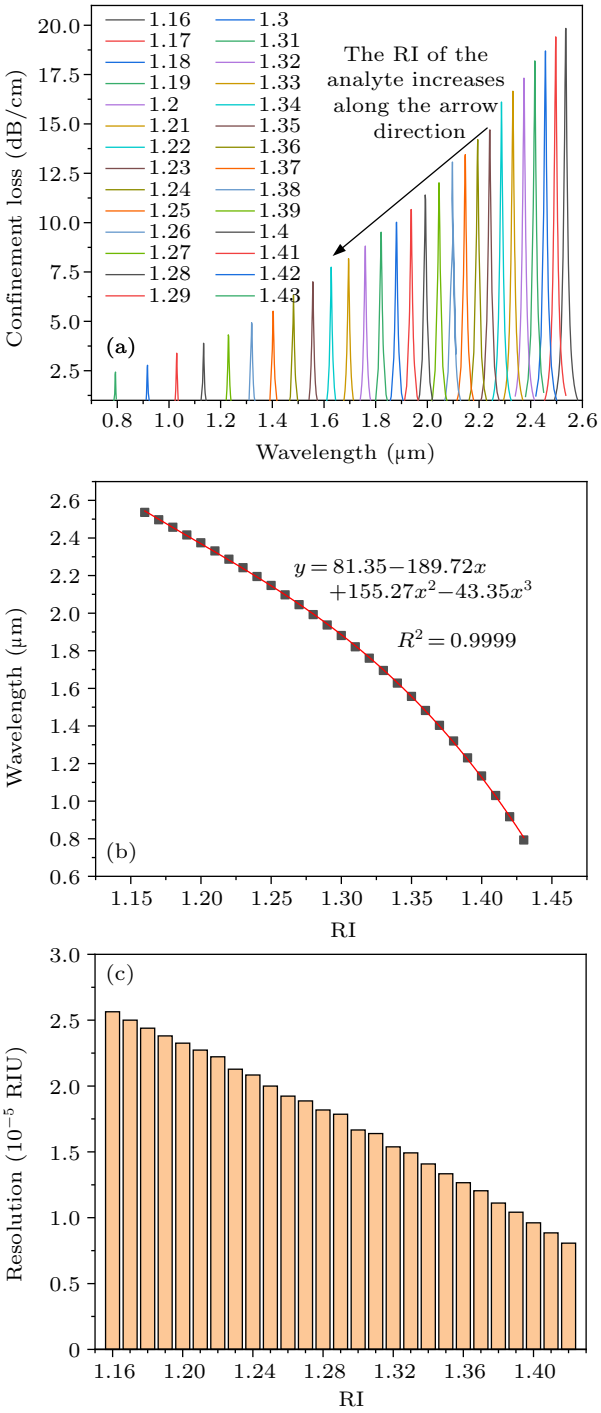


Fig. 8. (a) When the RI changes from 1.16 to 1.43, the confinement loss of the proposed TC-NCF sensor is plotted as a function of the wavelength. (b) The polynomial fitting function of the resonant wavelengths with respect to the RI. (c) The resolution of the proposed TC-NCF sensor under different analyte RIs.

larger when the RI is higher. The maximum and minimum resolutions obtained are 2.56×10^{-5} and 8.06×10^{-6}, respectively. The amplitude sensitivities of the TC-NCF sensor as a function of the wavelength for different RIs are shown in Figs. 9(a)–9(c). To obtain accurate numerical results, different RI changes are set in several RI ranges. The change in the RI Δn_a is set as 0.005 and 0.0025 in the range of 1.16–1.43. When the RI is fixed, the amplitude sensitivity of the TC-NCF sensor increases first and then decreases with the increase in the wavelength. The maximum amplitude sensitivity is -379.101 RIU^{-1} when the RI is 1.42. This is mainly because the transmission loss $\alpha(\lambda, n_a)$ suddenly increases near the resonant wavelength, which enhances the amplitude sensitivity according to Eq. (11). Table 1 summarizes the comparison results of the RI sensing performances of the TC-NCF with other reported works to comprehensively evaluate the sensing performances. According to Table 1, the proposed TC-NCF RI sensor has high sensitivity and resolution over an ultra-wide RI detection range of 1.16 to 1.43.

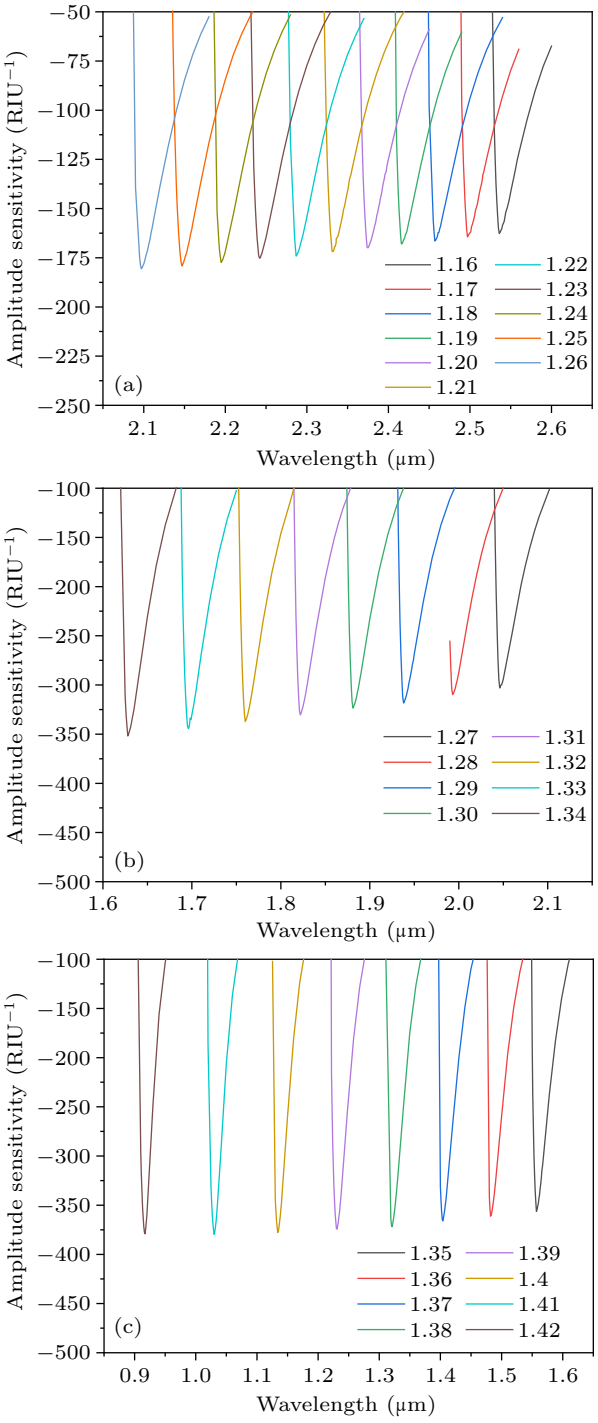


Fig. 9. The amplitude sensitivity as a function of the wavelength in the RI ranges of (a) 1.27–1.34 ($\Delta n_a = 0.005$), (b) 1.27–1.34 ($\Delta n_a = 0.0025$), and (c) 1.35–1.42 ($\Delta n_a = 0.0025$), respectively.

Table 1. Comparison results of the RI sensing performances of the TC-NCF with other reported works.

Refs.	Structures	RI range	Wavelength sensitivity (nm/RIU)	Amplitude sensitivity (RIU^{-1})	Resolution (RIU)
[24]	PCF filled with gold wires	1.29–1.49	4156.82	1056.33	2.41×10^{-5}
[15]	HC-NCF filled with gold wires	1.20–1.34	6100	N/A	2.63×10^{-5}
[25]	PCF with gold nanofilm	1.40–1.43	3978	N/A	N/A
[26]	PCF with air-core	1.33–1.41	11700	159.7	8.55×10^{-6}
[27]	dual-channel PCF	1.33–1.40	11600	N/A	8.62×10^{-6}
[28]	Au-coated dual-core PCF	1.33–1.51	6021	N/A	1.66×10^{-5}
This work	TC-NCF	1.16–1.34	12400	379.101	2.56×10^{-5}

The proposed TC-NCF structure is very simple; therefore, its fabrication process is not complex. It can be fabricated using the stack and draw technique.[29–31] Since it was proposed in 2019,[16] the truncated NCF has already been applied to polarized light transmission,[32] indicating that the fabrication technology of the truncated NCF is mature.

6. Conclusion

In summary, a TC-NCF RI sensor based on the SPR effect is proposed. The influences of the structural parameters on the propagation characteristics are investigated. With the proposed TC-NCF RI sensor, the ultra-wide RI detection range is from 1.16 to 1.43, the highest wavelength sensitivity reaches 12400 nm/RIU, and the R^2 of the polynomial fitting equation is 0.9999. Moreover, the maximum and minimum resolutions are 2.56×10^{-5} and 8.06×10^{-6}, respectively, and the maximum amplitude sensitivity can reach -379.1 RIU^{-1} when the RI is chosen as 1.43. The proposed TC-NCF RI sensor is expected to have substantial applications in biochemical medicine, environmental monitoring, and food safety.

Acknowledgment

Project supported by the National Natural Science Foundation of China (Grant No. 61935007).

References

[1] Vincetti L and Setti V 2014 *Opt. Express* **18** 23133
[2] Pryamikov A D, Biriukov A S and Kosolapov A F 2011 *Opt. Express* **19** 1441
[3] Debord B, Alharbi M, Bradley T, Fourcade-Dutin C, Wang Y Y, Vincetti L, Gérôme F and Benabid B 2013 *Opt. Express* **21** 28597
[4] Yu F, Wadsworth W J and Knight J C 2012 *Opt. Express* **20** 11153
[5] Kolyadin A N, Kosolapov A F, Pryamikov A D, Biriukov A S, Plotnichenko V G and Dianov E M 2013 *Opt. Express* **21** 9514
[6] Wei C, Weiblen R J, Menyuk C R and Jonathan H 2017 *Adv. Opt. Photon.* **9** 504
[7] Wei C, Young J T, Menyuk C R and Jonathan H 2019 *OSA Continuum.* **2** 2123
[8] Silva A A, Barea L, Spadoti D H and Francisco A C D 2019 *Opt. Eng.* **58** 072011
[9] Ankan I M, Mollah M A, Sultana J and Islam M S 2020 *Appl. Optics* **59** 8519
[10] Homola J 2008 *Chem. Rev.* **108** 462
[11] Xue J, Li S, Qin W, Xin X and Zhu X 2013 *Opt. Express* **21** 13733
[12] Hassani A and Skorobogatiy M 2006 *Opt. Express* **14** 11616
[13] Ding Z W, Lang T T, Wang Y and Zhao C L 2017 *J. Lightwave. Technol.* **35** 4734
[14] Yu Y L, Laiw S K, Kishikawa H and Goto N 2020 *Appl. Optics* **59** 5539
[15] Qiu S, Yuan J, Zhou X, Li F, Wang Q, Qu Y, Yan B, Wu Q, Wang K, Sang X, Long K and Yu C 2020 *Sensors* **20** 6539
[16] Wei C, Menyuk C R and Hu J 2020 *OSA Advanced Photonics Congress* NoM4G. 7
[17] Liu Y, Chen H, Ma M, Zhang W, Wang Y and Li S 2018 *J. Phys. D: Appl. Phys.* **51** 125101
[18] Ghosh G and Endo M 1994 *J. Lightwave. Technol.* **12** 1338
[19] Liu C, Lv J, Liu W, Wang F and Chu P K 2021 *Chin. Opt. Lett.* **19** 102202
[20] Santos D F, Guerreiro A and Baptista J M 2015 *IEEE Sens. J.* **15** 5472
[21] Paul A K, Sarkar AnK, Rahman A B S and Khaleque A 2018 *IEEE Sens. J.* **18** 5761
[22] Jiang L, Zheng Y, Hou L, Zheng K, Peng J and Zhao X 2015 *Opt. Commun.* **351** 50
[23] Hassani A and Skorobogatiy M 2007 *J. Opt. Soc. Am. B* **24** 1423
[24] Wang G, Lu Y, Duan L and Yao J 2020 *IEEE J. Sel. Top. Quantum Electron.* **27** 5600108
[25] Zhen K F, Fang S B, Li S G and Wei Z Y 2019 *Chin. Phys. B* **28** 094209
[26] Paul A K, Habib M S, Hai N H and Razzak S M A 2020 *Opt. Commun.* **464** 125556
[27] Bing P, Sui J, Wu G, Guo X, Li Z, Tan L and Yao J 2020 *Plasmonics.* **15** 1071
[28] Bing P B, Huang S C, Sui J L, Wang H and Wang Z Y 2018 *Sensors* **18** 2051
[29] Knight J C, Birks T A, Russell P S J and Atkin D M 1996 *Opt. Lett.* **21** 1547
[30] Knight J C 2003 *Nature* **424** 847
[31] Falkenstein P, Merritt C D and Justus B L 2004 *Opt. Lett.* **29** 1858
[32] Hong Y F, Gao S F, Ding W, Zhang X, Jia A Q, Sheng Y L, Wang P and Wang Y Y 2022 *Laser Photonics. Rev.* **16** 2100365